

# The Annulus-Filtered $E$ and $B$ Modes in CMBR Polarization

Tzihong Chiueh<sup>1</sup> and Cheng-Jiun Ma

Physics Department, National Taiwan University, Taipei, Taiwan

Received \_\_\_\_\_; accepted \_\_\_\_\_

submitted to ApJ

---

<sup>1</sup>Adjunct Research Fellow, Institute of Astronomy and Astrophysics, Academia Sinica, Taipei, Taiwan

## ABSTRACT

This work shows that the CMB polarization  $E$  and  $B$  modes can be measured in a clean manner in the real space by adopting a specific observing strategy: the detectors are configured to lie around a ring to observe an annulus of sky, where the antenna axis in each detector is oriented in the local radial direction. In particular, for the measurement of the weak  $B$  mode, the detector ring can be put in rotation about its axis. This additional degree of freedom allows each detector to directly measure the  $B$ -mode signal through long-term exposure to the sky without further data manipulation for removal of the  $E$  mode. We present the variances of the expected measured  $E$  and  $B$ -mode surface-brightness fluctuations as functions of the radius of the sky annulus. Both  $E$  and  $B$  modes have distinct features that can serve as the indicators for claiming detection. The temperature anisotropy- $E$  mode correlation can also be constructed by the present method, though it is probably not optimized.

*Subject headings:* cosmology; microwave background — polarization

## 1. Introduction

The CMB anisotropy provides direct information of the oldest relics of large-scale structures left from the Big-Bang. These CMB photons generally contain two types of information at every frequency band, the intensity and the polarization. Though the CMB photons are originated at the last scattering surface near red-shift  $z \sim 1000$ , they can be pre-processed and re-processed throughout the light path before reaching us, notably by the gravitational and Doppler effects. These effects dominantly affect the photon intensity, or the temperature anisotropy; they also affect the photon polarization only

to a much lesser degree. Thus, unlike the temperature anisotropy, it is believed that the CMB polarization can be a sensitive probe to the universe at a specific epoch when the photon temperature is about 3000 degrees and the photon optical depth  $\tau$  about 1/2. The CMB polarization is generated at this optical depth through the Thomson scattering of the pre-existing temperature anisotropy by the spatially homogeneous background of free electrons(Rees 1968; Bond and Efstathiou 1984; Polnarev 1985). Different types of normal modes in the primordial fluctuations result in different characteristics in the temperature anisotropy, thereby yielding different kind of polarization patterns. It has been pointed out that these different polarization patterns can be divided into two classes: the electric-type ( $E$ ) pattern and the magnetic-type ( $B$ ) pattern(Kamionkowsky et al. 1997; Zaldarriaga and Seljak 1997; Hu and White). The primordial density perturbations (scalar mode) generate only the  $E$  pattern, but the  $B$  pattern can be generated by the primordial gravitational waves (tensor mode). As the different patterns contain different physics, the ability to cleanly separate the  $E$  and  $B$  patterns has become a measure of success for future CMB polarization experiments.

Following the conventional approach to the temperature isotropy, most past works which address the CMB polarization tend to focus on how the two kind of patterns can be separated in the Fourier domain. Such an approach is natural for the whole-sky maps, such as those planned for the MAP and Planck missions. However, for the ground-based experiments, the whole-sky maps are impossible to obtain, and the adopted strategy is often the deep exposure of a small-patch of sky(Staggs et al. 1999; White et al. 1999; Lo et al. 2000). Unlike the whole-sky map, the local maps cannot naturally satisfy the periodic boundary conditions, and hence the brute-force Fourier analysis can often introduce distortion to the original data and produces un-desirable effects. For this reason, the real-space analysis of the local map is called for(Seljak and Zaldarriaga 1998; Chiueh 2000).

Recently, it has been proposed that with a suitable projection of the real-space data, one is able to separate the  $E$  and  $B$  patterns directly from the local map without recourse to the Fourier analysis(Chiueh 2000). This work also illustrates in a clear manner what the unfamiliar  $E$  and  $B$  patterns look like in the projected vector space. Though illuminating, this proposed projection, however, requires a differential operation on the data, which invariably amplifies the measurement noises significantly. Despite that the differentiation is afterward followed by a line integration to separate the  $E$  and  $B$  patterns, which tends to damp out the amplified noise, the damping can hardly balance the amplification. The combined effect thus leads to some level of noise amplification in the data. It is therefore desirable to pursue a different method that separates the  $E$  and  $B$  patterns in the real space without having to differentiate the data in the map.

In this previous work, it projects the polarization tensor into a vector and a pseudo-vector through differentiation, and then projects these vectors into a scalar and a pseudo-scalar through a line integration(Chiueh 2000). The scalar results from the  $E$  mode and the pseudo-scalar from the  $B$  mode. Following these ideas, we propose to project the polarization tensor into a vector and a pseudo-vector by replacing the differentiation by a multiplication with a position vector. These vectors finally get projected into a scalar and a pseudo-scalar, similarly, through a line integration. As will be shown later, the first step involves a non-trivial substitution. To be a valid operation for the  $E$ - $B$  separation, it imposes a constraint on the shape of the contour, along which the line integration is to carry out. This can be contrasted with the previously proposed method where no constraint should be imposed on the contour shape. Despite the constraint, the present analysis algorithm turns out to contain several good features in comparison with most previous methods.

This paper is organized as follows. Sec.(2) gives the formulation for the projection,

where the constraint on the shape of the integration contour is derived. The physical contents of the projection line integral with a contour of circular shape is examined in Sec.(3). Sec.(4) addresses the advantage of using this method for the measurement of the  $E$  pattern. Sec.(5) discusses the measurement strategy of the  $B$  pattern. Correlation of the  $E$ -mode polarization and the temperature anisotropy is addressed in Sec.(6). The conclusion is given in Sec.(7).

## 2. Projection Contour Integral

The polarization tensor  $\mathbf{P}$  can be expressed as

$$\begin{aligned}\mathbf{P} &= Q\sigma_x + U\sigma_y = [\nabla\nabla - (\hat{z} \times \nabla)(\hat{x}\nabla)]f + [\nabla(\hat{z} \times \nabla) + (\hat{z} \times \nabla)\nabla]g \\ &= Q + iU = 4\frac{\partial^2}{\partial\bar{w}^2}(f + ig)\end{aligned}\quad (1)$$

where  $\sigma_x$  and  $\sigma_y$  are the "3" and "1" components of the Pauli matrices, respectively, and  $f$  and  $g$  denote the  $E$  and  $B$  components, respectively. Moreover, from the third equality on, we have used a complex representation for  $\mathbf{P}$ , where  $w = x + iy$  and  $\bar{w} = x - iy$ . A convenient way to construct a scalar from  $\mathbf{P}$  proceeds as follows. Pick a closed contour  $C$  on the polarization map, contract the tensor  $\mathbf{P}$  with a suitable local tensor to form a scalar/pseudo-scalar at every point on the contour, and then sum up these scalar quantities over the contour to obtain a contour-integrated value. Mathematically, the operation can be written as

$$Y \equiv 4 \int_C \frac{\partial^2(f + ig)}{\partial\bar{w}^2} \bar{w} d\bar{w}. \quad (2)$$

where  $\bar{w} d\bar{w}$  is the local tensor for projecting out the scalar  $Y$ ,  $C$  is the closed contour along which the line integration is performed, and the coordinate  $\bar{w}$  can be chosen so that the origin is inside the contour. In terms of the Stokes  $Q$  and  $U$ , Eq.(2) is

$$Y = \int_C [(xQ + yU)dx - (yQ - xU)dy] - i \int_C [(yQ - xU)dx + (xQ + yU)dy]. \quad (3)$$

Considering the fact that  $\bar{w}\partial^2 A/\partial\bar{w}^2$  can be expressed as a total derivative, equal to  $\partial[\bar{w}(\partial A/\partial\bar{w}) - A]/\partial\bar{w}$ , and that  $f$  and  $g$  are both analytical functions, we arrive at the following expression for  $Y$  of Eq.(2),

$$Y = i \int_C \left[ \frac{\partial D}{\partial y} dx - \frac{\partial D}{\partial x} dy \right], \quad (4)$$

where  $D \equiv \bar{w}(\partial(f + ig)/\partial\bar{w}) - (f + ig)$ . Using the Stokes theorem and the fact that  $\nabla^2 = 4\partial^2/\partial\bar{w}\partial w$ , Eq.(4) can further be rewritten as

$$Y = -i \int \nabla^2 D d^2 S = -i \int \bar{w} \frac{\partial}{\partial \bar{w}} \nabla^2(f + ig) d^2 S, \quad (5)$$

where the surface integration is confined within the area bounded by the contour  $C$ . Instead of placing an integration limit for the surface integral, we may multiply the integrand of Eq.(5) by a top-hat filter function  $W(x, y)$  and carry out the surface integral without an explicit bound, where  $W(x, y) = 1$  inside the contour  $C$  and it vanishes otherwise. This permits a convenient way to evaluate the second equality of Eq.(5). Note that  $\bar{w}\partial/\partial\bar{w} = (\partial/\partial\ln r) + i(\partial/\partial\phi)$  in the polar coordinate. With an integration by part, Eq.(5) becomes

$$Y = i \int \left[ \frac{\partial W}{\partial \ln r} + 2W + i \frac{\partial W}{\partial \phi} \right] \nabla^2(f + ig) r dr d\phi. \quad (6)$$

Note that  $W$  is a real quantity and before the integration, Eq.(6) itself can not yield the  $E$  and  $B$ -mode separation through identifying each mode with the real or imaginary part of the integrand. However, after the surface integration, it is now possible to give rise to a  $Y$  such that the real or imaginary parts can be identified as the  $B$  or  $E$  mode. This can be made possible only if we choose  $r^2 W$  to depend only on either  $r$  or  $\phi$ , but not both. But, the choice of  $\phi$  dependence yields an undesirable  $W$  which is not compact.

This leaves the one and only one choice for the contour so that  $W(x, y) = W(r) = \Theta(R - r)$ , a circular top-hat filter function. That is, the scheme for projecting the polarization tensor into a suitable scalar/pseudo-scalar, i.e., Eq.(2), can only be possible

when we choose the integration contour to be a circle. Such a choice yields the real part of  $Y$  to be entirely contributed by the  $B$  mode and the imaginary part of  $Y$  by the  $E$  mode. It also leaves  $Y$  to depend on the only one degree of freedom for the circle, i.e., the radius  $R$ .

### 3. $E$ - $B$ Separation through a Circular Filter

Let the circular contour to have a radius  $R$  and center at  $\mathbf{x}_0$ ,

so that  $r \equiv |\mathbf{x} - \mathbf{x}_0|$ . It then follows from Eqs.(3) that

$$\begin{aligned} Y(R; \mathbf{x}_0) &= -iR^2 \int_0^{2\pi} [(\cos(2\phi)Q + \sin(2\phi)U) + i(\cos(2\phi)U - \sin(2\phi)Q)]d\phi \\ &= -iR^2 \int_0^{2\pi} [(r \frac{\partial}{\partial r}(\frac{1}{r} \frac{\partial}{\partial r}) - \frac{1}{r^2} \frac{\partial^2}{\partial \phi^2})(f + ig) - \frac{2}{r} \frac{\partial}{\partial \phi}(\frac{\partial}{\partial r} - \frac{1}{r})(g - if)]d\phi \\ &= i \int_0^{2\pi} \int_0^\infty \bar{W}(r) \nabla^2(f(\mathbf{x}) + ig(\mathbf{x})) r dr d\phi, \end{aligned} \quad (7)$$

where the second equality can be straightforwardly derived from Eq.(2) and the third equality is simply Eq.(6) with a filter function  $\bar{W} \equiv (1/r)d(r^2W)/dr$ . The angular factors on the right of the first equality in Eq.(7) is a familiar one. It is nothing more than a description of how the tensor components  $Q$  and  $U$  rotate as the coordinate rotates. In fact in this integrand the polarization vector  $\mathbf{P}$  is rotated to  $Q_0 + iU_0$  of a preferred coordinate  $(x_0, y_0)$ , where the  $x_0$ -direction is aligned with the local radial direction of the circle and the  $y_0$ -direction aligned with the local azimuthal direction. It is important to notice that the separation of  $E$  and  $B$  modes depends critically on a perfect angular integration, which yields a real part given by the angular average of  $\partial^2 f / \partial r^2 - (1/r) \partial f / \partial r$  and an imaginary part given by the angular average of  $\partial^2 g / \partial r^2 - (1/r) \partial g / \partial r$ . Similar expressions for Eq.(7) have also been derived recently(Seljak and Zaldarriaga 1998; Crittenden et al. 2000) based on a related idea for weak lensing studies(Kaiser et al 1994).

From Eq.(2), it is clear that  $Y$  can be measured by configuring all detectors to lie on an

one-dimensional ring, and each detector observes a small part of a sky annulus of radius  $R$ , since the interior to the annulus is not needed for the measurement. Furthermore, according to Eq.(7), the linear antennae (or their equivalents) in the detectors at different positions on the ring should be oriented in such a way that the two principal axes are in the local radial and azimuthal directions for the polarization measurement. This detector configuration turns out to be a very useful one if there can be an extra degree of freedom installed to the experiment, rotation about the axis of the ring. As will be discussed in Sec.(5) for the  $B$ -mode measurement, this extra degree of freedom makes the perfect angular integration of Eq.(7) possible, thereby allowing the  $B$  mode to be extracted from the polarization measurement.

On the other hand, we may examine what the physical contents of  $\nabla^2 f$  and  $\nabla^2 g$  in Eq.(7) are. It becomes clear when we look into their respective power spectra, i.e.,  $k^4|f_k|^2$  and  $k^4|g_k|^2$ , where  $f_k$  and  $g_k$  are the Fourier components of  $f$  and  $g$ , respectively. Each power spectrum equals the corresponding power spectrum of polarization:

$$\langle |Q_k|^2 \rangle + \langle |U_k|^2 \rangle = k^4|h_k|^2, \quad (8)$$

where  $Q_k$  and  $U_k$  are the  $E$  or  $B$  contribution to the Fourier components of  $Q(\equiv (\partial^2/\partial x^2 - \partial^2/\partial y^2)f - 2(\partial^2/\partial x\partial y)g)$  and  $U(\equiv (\partial^2/\partial x^2 - \partial^2/\partial y^2)g + 2(\partial^2/\partial x\partial y)f)$ , respectively, and  $h$  can be either  $f$  or  $g$ . This is interesting since the scalar  $\nabla^2 f$  or  $\nabla^2 g$  has the same power spectrum as that of the corresponding polarization tensor, and hence the proposed contour integration contains some gross information of the conventional  $E$  and  $B$ -mode power spectra constructed directly from the Stokes parameters.

Moreover, since  $Y_h(R; \mathbf{x}_0)$  is a random number as the circle may be centered at various locations  $\mathbf{x}_0$ , the variance of  $Y$  can be expressed as:

$$(2\pi R^2)\Delta T_h(R) \equiv \langle Y_h^2(R; \mathbf{x}_0) \rangle_{\mathbf{x}_0}^{1/2} = \left[ \int_0^\infty |\bar{W}_k|^2 \frac{k^4|h_k|^2}{2\pi A} k dk \right]^{1/2}, \quad (9)$$

where  $\bar{W}_k$  is the Fourier component of  $\bar{W}$ ,  $\langle \dots \rangle_{\mathbf{x}_0}$  stands for the ensemble average of various  $\mathbf{x}_0$ , and  $A$  for the area of the map. Here,  $\Delta T_h$  denotes the measured variance of the polarization brightness temperature (or flux surface density) for mode  $h$ , and the factor  $2\pi R^2$  in Eq.(9) arises from the product of two factors: a factor  $R$ , which we have multiplied to the data for constructing  $Y_h$  in Eq.(2), and the circumference  $2\pi R$  of the sky annulus, which needs to be divided away to obtain the flux density. That is, the measured  $\Delta T_h(R)$  contains the polarization spectral information of either mode, subject only to the smearing by a  $k$ -space filter  $|\bar{W}_k|^2$ .

The length scale of smearing depends on the radius  $R$ , but the details of smearing depend on the power spectrum of the filter function  $|\bar{W}_k|^2$ .

Since  $\bar{W}$  consists of a top-hat disk and a thin shell, its power spectrum oscillates in the  $k$  space at a particular phase with a well-defined frequency comparable to  $2R$ , the Gibb's phenomenon, and the oscillation amplitude declines as  $k^{-1}$ .

#### 4. Detection of the $E$ Mode

At the first glance, it appears that such a  $k$ -space smearing is too extended to be useful. However, this disadvantage may be turned into an advantage for the polarization measurement. In the standard Cold-Dark Matter cosmogony, the power spectrum of  $E$  mode also oscillates in the  $k$  space with well-defined frequency and phase. This allows for the possibility that one may adjust the smoothing radius  $R$  to control the oscillation frequency in the power spectrum of  $\bar{W}$  so as to optimize the detection of  $E$ -mode signals. In principle, one would like to have the two oscillations match in frequency to maximize the overlap of  $|\bar{W}_k|^2$  and  $|h_k|^2$  in Eq.(9). However, this does not necessarily produce the maximal power, as two oscillations may be out of phase, giving destructive interference.

The phase of the  $k$ -space oscillation in the  $E$ -mode power spectrum is such that it always oscillates asymptotically like  $\sin(2\pi k/S)$  for  $k/S \geq 2$ , and this behavior is rather insensitive to the cosmological parameters, such as  $\Omega_0$  and  $\Omega_\Lambda$ , where  $S$  is the oscillation period, the only cosmological-parameter-dependent quantity. Most power of  $k^2(|Q_k|^2 + |U_k|^2)$  in the  $E$ -mode is in fact contained in between  $k/S = 2$  and  $k/S = 5$  where the approximation is good.

It is fortunate that  $|\bar{W}_k|^2$  has a right phase such that it also oscillates like  $\sin(2kR)$ . This will be shown below. By adjusting the smoothing radius  $R$  so that  $R \approx 2\pi/S$ , we can obtain significant overlap of  $|\bar{W}_k|^2$  and  $|h_k|^2$ , whereby considerable power of the  $E$  polarization in the measured map can be extracted. We now turn to showing that  $|\bar{W}_k|^2 \sim \sin(2kR)/k$  at a large  $kR$ .

The two dimensional Fourier transformation of  $\bar{W}$  is

$$\begin{aligned}
 \bar{W}_k &= \int [2\Theta(R-r) - r\delta(r-R)] e^{ikr \cos(\phi-\phi_k)} d^2\mathbf{r} \\
 &= \int_0^\infty r dr [2\Theta(R-r) - r\delta(r-R)] \int_0^{2\pi} d\phi \sum_n J_n(kr) e^{in(\pi/2+\phi_k-\phi)} \\
 &= 2\pi \int_0^\infty r dr J_0(kr) [2\Theta(R-r) - r\delta(r-R)] \\
 &= 2\pi R^2 [2\frac{J_1(kR)}{kR} - J_0(kR)],
 \end{aligned} \tag{10}$$

where the first term of the last equality arises from the disk and the second term from the shell. The two can be combined to become  $2\pi R^2 J_2(kR)$ . For  $kR \geq 2\pi$ ,  $J_2(kR)$  oscillates as  $-\cos(\pi/4 - kR)/\sqrt{kR}$ . Thus,  $|\bar{W}_k(kR)|^2$  asymptotically oscillates at a twice frequency  $2R$  as  $\sin(2kR)/k$  about a background of half the oscillation amplitude.

To illustrate how the filter function  $\bar{W}_k$  captures the oscillating  $E$  mode power spectrum, we show  $|\bar{W}_k|^2$  for suitably chosen  $R$  in Fig.(1a), (1b) and (1c), in comparison with the

$E$ -mode power spectra of the  $\Lambda$ CDM model with  $\Omega_\Lambda = 0.7$ ,  $\Omega_m = 0.28$  and  $\Omega_b = 0.02$ , the standard flat CDM model and the open CDM model with  $\Omega_m = 0.28$  and  $\Omega_b = 0.02$  respectively. Instead of using  $k$ , we have used the conventional spherical-harmonics mode number  $l$  as the horizontal axis. We identify  $\mathbf{r}$  to be the angle on a flat sky, and the relation between  $k$  and  $l$  is  $l \approx k$  for a large  $l$ . Moreover, the conventional power spectrum  $l^2 C_{E,l} / 2\pi$  in the spherical harmonic space is replaced by  $k^4 |f_k|^2 / 2\pi A$ .

Shown in Fig.(1) are also  $|\bar{W}_k|^2$  for a different choice of  $R$ , where the first lobe of  $J_2(kR)^2$  is just large enough to enclose the major peaks in the  $E$ -mode power spectrum. Such an annulus radius is about a factor of  $3 - 4$  smaller than the choice of  $R$  that matches the  $E$ -mode oscillation.

These are the two specific  $R$ 's that are expected to capture a substantial power of the  $E$  mode.

We next plot the squared variance of the measured  $\Delta T_E$  as a function of the annulus radius  $R$  in Fig.(2) for the  $\Lambda$ CDM, standard flat-CDM and open-CDM cosmologies, where  $R$  is expressed in unit of arcminute. The primary peak of the polarization brightness corresponds to the small one of the two specific  $R$ 's shown in Fig.(1). This is expected because the first lobe of  $J_2^2$  captures a great deal of the  $E$ -mode power. The optimal  $R$ 's that give rise to the peaks in Fig.(2) capture about  $1/4$  of the total  $E$ -mode power for the three cosmologies; each is slightly larger than, or comparable to, the power contained within the most dominant peak shown in Fig.(1a), (1b) or (1c).

There exists a second peak, which is not clearly visible in the plots as it blends with the primary peak, and this second peak comes from the larger  $R$  which produces the oscillating  $|W_k|^2$  that matches the oscillation pattern in the  $E$ -mode power spectrum. Apart from the contributions from the two peaks, the E-polarization brightness is seen to drop rapidly

toward large and small  $R$ . The  $\Lambda$ CDM and standard flat-CDM cosmologies can hardly be distinguishable at the primary peak except for their different heights. However, thanks to the existence of the particular larger  $R$  discussed above, the two cosmologies have different second peaks, allowing them to be differentiated in the  $E$ -mode measurement.

On the other hand, the open-CDM cosmology is distinct from the other two in both the peak position and height.

### 5. Observational Strategy for $B$ Mode: Rotating Detector Ring

Though the last section has shown the promise of this proposed method for the  $E$ -mode measurement, a naive application of this method to the  $B$ -mode measurement may prove to be much more difficult to realize. As the detection of the  $B$  mode offers a much greater scientific return, it thus poses the grand challenge for all CMB polarization experiments in the foreseeable future. The main challenge here is to defeat the noise and the spillover from the much stronger  $E$  mode. In this regard, the  $B$ -mode measurement can be a completely different experiment from the  $E$ -mode measurement, and it may require very different detector designs and observational strategies. Here, we shall discuss how the present projection method with detectors configured in a ring can be extended to the much more difficult  $B$ -mode measurement, provided that a more sophisticated observational strategy is adopted.

The  $E$ -mode surface brightness per log-waveband (i.e.,  $\log k$ ) peaks at the angular scale about  $10 - 20$  arc-minutes for the currently most favorable  $\Lambda$ CDM cosmology, c.f., Fig.(1a). On the other hand, the surface brightness for the  $B$ -mode per log-waveband is about 10% of that for the  $E$ -mode and peaks on the angular scale of a couple of degrees. It is fortunate that the  $B$ -mode power concentrates at a much larger scale than where the

$E$ -mode power does by almost one order of magnitude. The scale separation thus offers a possibility that the weak  $B$  mode may be extracted from the CMB polarization in the presence of the strong  $E$  mode.

First of all, we note that the projection, Eq.(2), (3) or (7), involves no differentiation of the measured data, which is invariably contaminated by the small-scale noise. The line integration/summation of the data in fact helps suppress the small-scale, pixel-size noise by a factor of  $N^{-1/2}$ , where  $N$  is the number of detectors on the detector ring. The present method for extracting  $E$  and  $B$  modes directly from the measured  $Q$  and  $U$  works better than the previously proposed method(Chiueh 2000), in that it avoids the differential operation on the data, which is necessary for the previous proposal to project out two topologically distinct vectors from the polarization tensor.

There is however a caveat for the present method. We concluded in Sec.(2) that the contour of the projection line integration/summation must be a circle in order for  $E$  and  $B$  modes to be cleanly separated. However, the real-space measurements collect photons in discrete detectors. Having a finite number of detectors, one must interpolate the measured data in between adjacent detectors to perform the circular-line integration. In this regard, it is preferable that the detectors are configured to be closely packed on a circle to reduce the interpolation errors. Unfortunately, the small real part of  $Y$  (the  $B$  mode) in Eq.(7) arises from the small residue of cancellation among the  $N$  much larger quantities ( $E$ -mode contribution) over the summation of  $N$  detectors, as noted from the second equality of Eq.(7). This further demands the detector configuration to be well-designed and the data analysis to take extreme care.

The above considerations point to the critical need for performing a nearly perfect line integration described in Eq.(7) in order for the  $B$  mode not to be plagued by the spillover from the  $E$  mode. One possible observational strategy, or design of detector configuration,

to achieve this goal is that the detector ring can be continuously rotating about its axis which tracks the sky. It permits uniform exposure of all detectors to the observed sky annulus. In addition, the angular integration is now translated to time integration. As each detector traces an exact circle, the time (or angular) integration can be performed within each detector. The spillover of  $E$ -mode to the  $B$ -mode can in principle be completely removed when the rotating detectors are in use, as will be discussed shortly. A related gain of such an observational strategy is that the calibration of the detector response across all detectors does not need to be conducted as frequently as in the case with a static ring. There is no longer a need to fill the ring with closely packed detectors and the signals collected by each detector after a long integration can be straightforwardly summed together.

The scale separation of  $E$  and  $B$  modes now yields the  $E$ -mode time-variation with wide-band frequencies about 10 times higher than that of the  $B$  mode. The present projection method is nothing more than to extract the dc component out of the signals. The amplitude of the ac signal of frequency  $\omega$  after a period  $T$  of integration is reduced by a factor  $(\omega T)^{-1}$ , suggesting that the  $E$ -mode contribution that contaminates the  $B$  mode in the integrand of Eq.(7) can be substantially reduced to an amplitude comparable to that of the  $B$  mode after one period of rotation. Therefore, apart from the instrumentation errors, the  $E$ -mode spillover can be satisfactorily removed after many rotation periods. Notice that the nice feature of this method that maps the spatial patterns into time variation results entirely from the fact that the detectors are configured in a ring and measure a sky annulus. The signals are spatially periodic, and this topology and symmetry of the data set permits one to manipulate the data free of problems pertaining to the boundaries.

Fig.(3 a, b, c) shows how the best choice of  $|W_k(R)|^2$  captures the  $B$ -mode power spectra for the three cosmologies indicated in Fig.(1). Fig.(4) shows  $\Delta T_B(R)^2$  for the three kind of cosmologies indicated in Fig.(1). We note that the peak power is also comparable to

the power contained in the peak of the  $B$ -mode spectrum shown in Fig.(3), and it captures about 1/5 of the total  $B$ -mode power for the three cosmologies.

We now turn to brief discussions on the potentially most serious contaminants to the  $B$ -mode measurement. The contamination of the scattered polarized photons from the terrestrial environments, such as the 3-degree CMB photons reflected by the ground and observational instruments, can pose a serious problem for the polarization measurement, and is even more so for the  $B$ -mode measurement. Nevertheless, uniform illumination of polarized photons to the detector annulus can contribute no net polarization signal after a perfect line integration as the first equality of Eq.(7) shows; neither can the dipole pattern of illumination sources. In fact, among all multipole patterns, only the quadrupole patterns can contribute to the polarization measurement for the scheme that this work proposes, and serious measures must be taken for removing this kind of scattered light in the experiment.

The confusion from polarized point sources can also be a serious concern for the CMB polarization measurement, as they generally contain quadrupole moments and contribute to both  $E$  and  $B$  modes. However, since the present method measures small patches of sky in the real space, it is possible to identify the point-source suspects, the non-Gaussian features, from the data and remove the point sources. Thus, the point-source confusion can thus be a solvable problem by the present observing method.

## 6. Temperature Anisotropy-Polarization E-Mode Correlation

The  $E$ -mode polarization in the CMBR results from the Thomson scattering off the temperature anisotropy of the primordial adiabatic and/or iso-curvature fluctuations. Therefore, the polarization  $E$ -mode is causally related to the temperature anisotropy, with its phase locked to temperature fluctuations. The correlation between the temperature

anisotropy scalar field and the polarization tensor field is conventionally defined in the Fourier space as  $C_{TE,k} = -k^2 \langle \text{Re}[k^2 f_k T_k^*] \rangle$  per  $\log(k)$  band, where  $\langle \dots \rangle$  denotes the angular average for the direction of the wave-vector  $\mathbf{k}$ . Plotted in Fig.(5,a,b,c) are  $C_{TE,k}$  of the same three cosmologies as those indicated in Fig.(1). The averaged signals are a factor of few stronger than those of the  $E$  polarization. In the real space, the inverse Fourier transformation gives

$$C_{TE}(r) = \int \frac{d^2 \mathbf{x}_0}{A} \nabla^2 f(\mathbf{r} + \mathbf{x}_0) \Delta T(\mathbf{x}_0). \quad (11)$$

An experiment that is equipped with detectors of full-polarization capability can measure all four Stokes parameters at the same time. When the detectors are configured in a ring and the signals from all detectors are summed together, the measured Stokes parameters will all be subject to the smearing of some filter functions. Thus, this proposed observational strategy produces a different representation of  $T - E$  correlation from  $C_{TE,k}$  and  $C_{TE}(r)$  described above. While the filter function for the polarization tensor field is  $\bar{W}$ , the filter function  $W_s$  for the  $\Delta T$  scalar field is a different one, i.e.,  $W_s(r; R) = r\delta(r - R)$ . The Fourier component of  $W_s(r; R)$  is  $W_{s,k}(R) = 2\pi R^2 J_0(kR)$ , simply replacing  $J_2$  of  $\bar{W}_k$  by  $J_0$ .

With the same spirit for the variance of  $E$  and  $B$  modes, we define the  $T - E$  correlation by multiplying the measured  $Y_E$  on the annulus with the temperature anisotropy measured by the same annulus. The filter-weighted  $T - E$  correlation, in unit of temperature, is thus

$$\begin{aligned} \bar{C}_{TE}(R) &= (2\pi R^2)^{-2} \langle Y_E(R; \mathbf{x}_0) \int W_s(r; R) \Delta T(\mathbf{x}_0 + \mathbf{r}) d^2 \mathbf{r} \rangle_{\mathbf{x}_0} \\ &= - \int_0^\infty k^2 \frac{\text{Re}[f_k T_k^*]}{2\pi A} J_0(kR) J_2(kR) k dk. \end{aligned} \quad (12)$$

Plotted in Fig.(5 a, b, c) are also the composite filter function  $J_0(kR) J_2(kR)$  of some choice of  $R$  for the three cosmologies. Figure (6) shows  $\bar{C}_{TE}(R)$  as functions of  $R$  in unit of arcminute. As  $C_{TE}(r)$  is not a positive definite quantity and the spatial filtering tends

to smear out the  $T - E$  correlation, it is seen from a comparison with Fig.(5) that the resulting  $\bar{C}_{TE}$  gives rise to a relatively small signal strength for all filter sizes  $R$ . Thus, the above straightforward multiplication of the filtered temperature anisotropy with the filtered  $E$ -mode polarization is probably not an optimal operation, and the optimal one still needs to be found. Nevertheless, if an experiment has a sufficiently high sensitivity to detect the  $E$ -mode variance, it should also be within its capability to measure the  $T - E$  correlation,  $\bar{C}_{TE}$ , as their surface brightness is comparable.

## 7. Conclusion

This work addresses how the CMBR polarization  $E$  and  $B$  modes can be separated in a local map of Stokes parameters  $Q$  and  $U$ . The present method needs only the data on a sky annulus. Thus, the  $N$  detectors can be configured to lie on a circle measuring an annulus of the sky of radius  $R$ ; by varying  $R$ , one can measure the  $E$  and  $B$  modes of various scales. Though such a detection strategy contains only some gross information of the power spectrum, it nevertheless exhibits the following good features:

- (a) The measurement is in the real space, and it is sensitive to the spatially localized non-Gaussian features.

Some of the non-Gaussian features are the polarized point sources, and they can potentially be identified and removed.

- (b) The measurement can be conducted on a turntable and each detector can perform its own circular integration through the time integration of the measured Stokes  $Q$  and  $U$ . It is essential for the weak  $B$ -mode measurement to be equipped with a rotating detector ring. On one hand, it avoids the need for frequent detector calibration (i.e., flat field), thereby making the observation much more stable and easier, and on the other hand it can

in principle completely remove the contamination from the much stronger  $E$  mode and increase the signal-to-noise ratio by straightforwardly summing up all signals collected by the  $N$  detectors on the ring. This observing strategy still works even when the measured sky annulus has a non-negligible width so that Eq.(10) can no longer hold. It is because the signals collected by the detectors after many periods of rotation can always remain axi-symmetric, which is essential for the  $E$ - $B$  separation.

- (c) The polarized CMB  $E$ -mode flux collected by this method is comparable to that adopting the conventional observational strategy that measures a particular peak of the power spectrum, which is limited by the narrow peak width.
- (d) The present method measures, in effect, the circular-top-hat-filtered polarization patterns. In the Fourier domain, the power spectra of both the top-hat filter and the polarization  $E$  mode oscillate. The present method provides a filter of size  $R$  for the two oscillations to have the same frequencies and phases, so that a non-negligible power of the  $E$  mode can be captured. It offers an additional feature for differentiating the  $\Lambda$ CDM cosmology from the standard flat-CDM cosmology, beside the different heights of the primary peaks shown in Fig.(2).

In sum, with the above advantages and the existence of the distinct features in  $\Delta T_E(R)$   $\Delta T_B(R)$  and  $\bar{C}_{TE}(R)$ , the present real-space analysis provides a new and efficient way to detect the CMBR polarization for those ground-based or balloon-borne experiments, where the observation is confined within a small patch of sky.

This work is supported in part by the National Science Council of Taiwan under the grant NSC89-2112-M-002-065.

## REFERENCES

Bond, J.R. & Efstathiou, G. 1984, ApJ, 285, L45

Chiueh, T. 2000, arXiv:astro-ph/0010433

Crittenden R.G., Natarajan P., Pen, U.L. & Theuns, T., 2000, arXiv:astro-ph/0012336

Hu, W. & White M. 1997, Phys. Rev. D56, 596

Kaiser, N., Squires, G., Fahlman, G., Woods, D. 1994, in "Cluster of Galaxies" eds. F. Durrett, A. Maxure, and J. Tran Thanh Van, Editions Frontieres, Gif-sur-Yvette, p.269

Kamionkowsky, M., Kowsowsky, A. & Stebbins, A. 1997, Phys. Rev. D55, 7368

Lo, K.Y., Chiueh, T., Liang, H., Ma, C.P., Martin, R., Ng, K.-W., Pen, U.L. & Subramanyan, R. 2000, IAU Symp. no. 201, 31

Polnarev, A.G. 1985, Sov. Astron., 29, 607

Rees, M.J. 1968, ApJ, 153, L1

Seljak, U. & Zaldarriaga, M. 1998, in "Fundamental Parameters in Cosmology" proceedings of the XXXIIrd Rencontres de Moriond 1998, arXiv:astro-ph/9805010

Staggs, S.T., Gunderson, J.O. & Church, S.E., 1999, arXiv:astro-ph/9904062

White, M., Carlstrom, J. E., Dragovan, M., Holzapfel, W. L. 1999, ApJ, 514, 12

Zaldarriaga, M. & Seljak, U. 1997, Phys. Rev. D55, 1830

Fig. 1.— The power spectra of  $E$ -modes  $l(l+1)C_{E,l}/2\pi$  (solid lines) for the (a)  $\Lambda$ CDM with  $(\Omega_\Lambda, \Omega_m) = (0.7, 0.28)$ , (b) standard flat-CDM, and (c) open CDM cosmologies. Superposed on the power spectra are the (arbitrarily scaled)  $k$ -space filter functions  $|\bar{W}_k(R)|^2$  of two particular annulus radii  $R$  (dotted and dashed lines), which are optimized to capture the features in the power spectra.

Fig. 2.— The squared variances  $\Delta T_E^2$  as functions of the annulus radius  $R$  for the three cosmologies of Fig.(1). The three arrows show the total  $E$ -mode power for the three cosmologies.  $\Delta T_E^2$  is in unit of  $\mu K^2$  and  $R$  in unit of arcminute.

Fig. 3.— The power spectra of  $B$  modes  $l(l+1)C_{E,l}/2\pi$  (solid lines) for the three cosmologies of Fig.(1). Superposed on the power spectra are the (arbitrarily scaled)  $k$ -space filter functions of the optimized  $R$ 's that capture the power of the  $B$  modes (dotted lines).

Fig. 4.— The squared variances  $\Delta T_B^2$  as functions of  $R$  for the three cosmologies. The three arrows show the total  $B$ -mode power. The units are the same as Fig.(2).

Fig. 5.— The  $T - E$  correlation spectra  $l(l+1)C_{TE,l}/2\pi$  (solid lines) for the three cosmologies. Superposed on the correlation spectra are the (arbitrarily scaled)  $k$ -space filter functions for some choice of  $R$ 's. Hardly can any choice of  $R$  yield  $k$ -space filter functions that oscillate in phase with the correlation spectra.

Fig. 6.— The filtered  $T - E$  correlation  $\bar{C}_{TE}$  as functions of  $R$  for the three cosmologies. The units are the same as Fig.(2). The signal strengths are seen to be substantially lower than the peaks in Fig.(5).

Fig. 1a

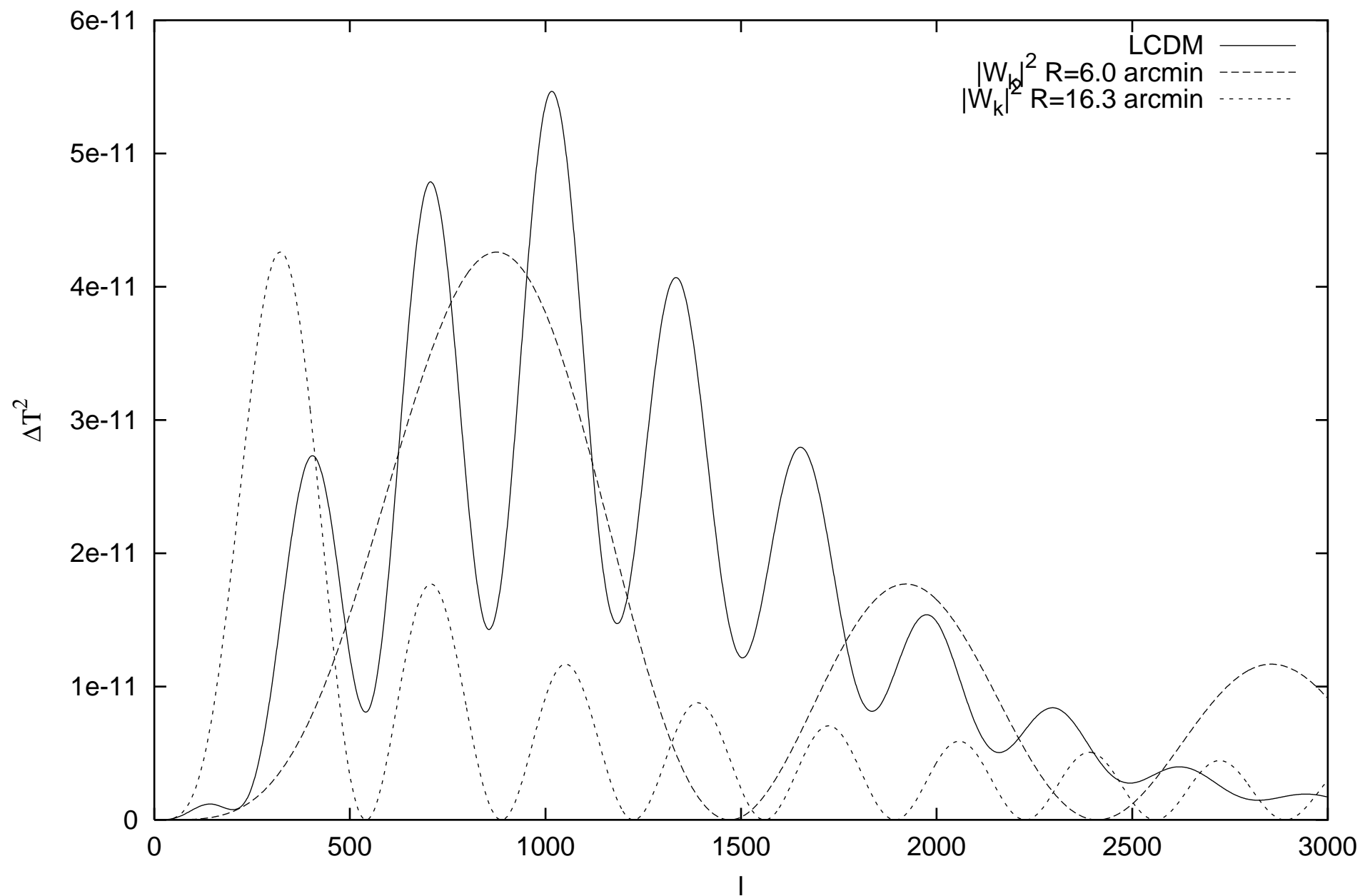


Fig. 1b

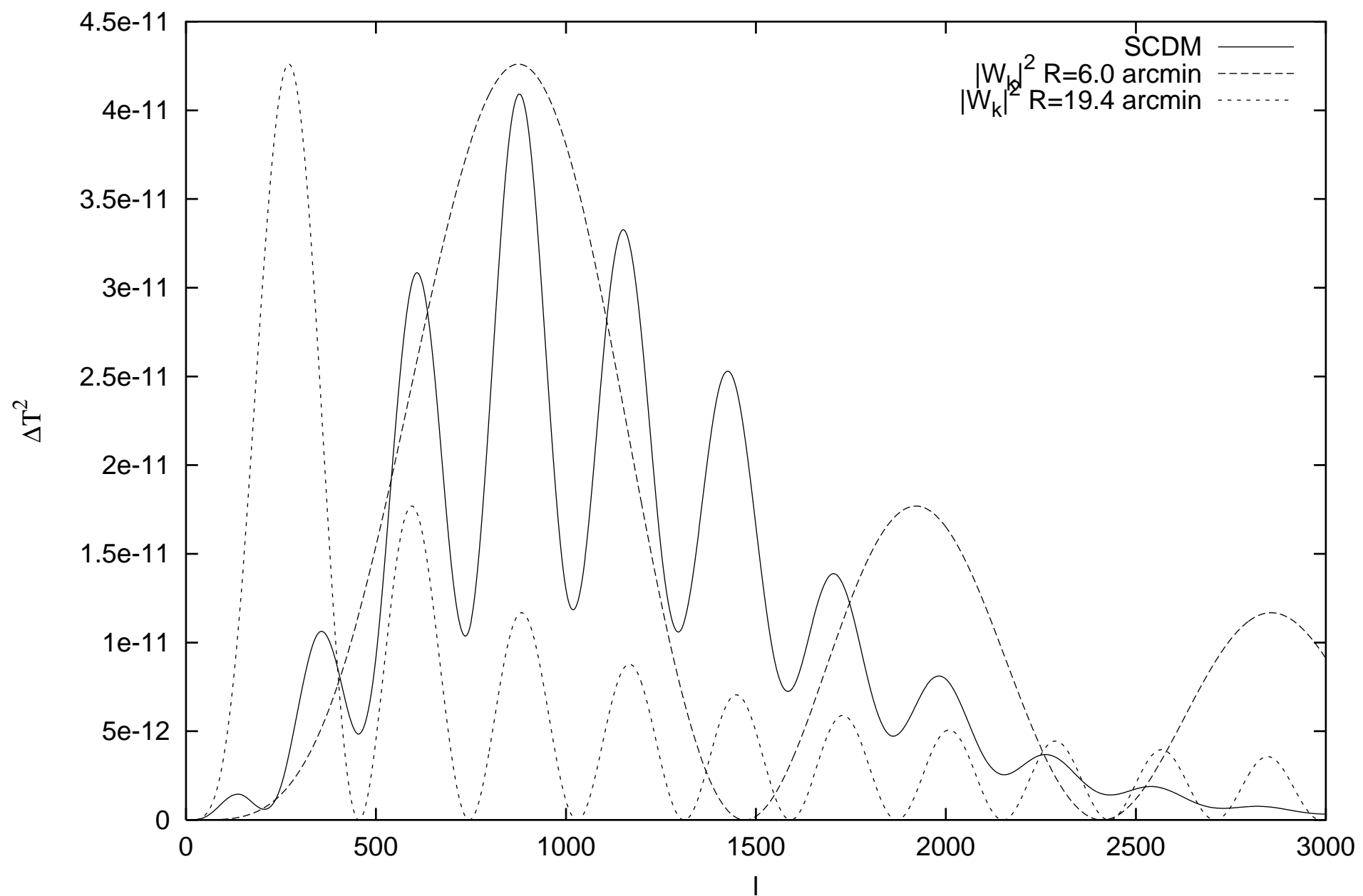


Fig. 1c

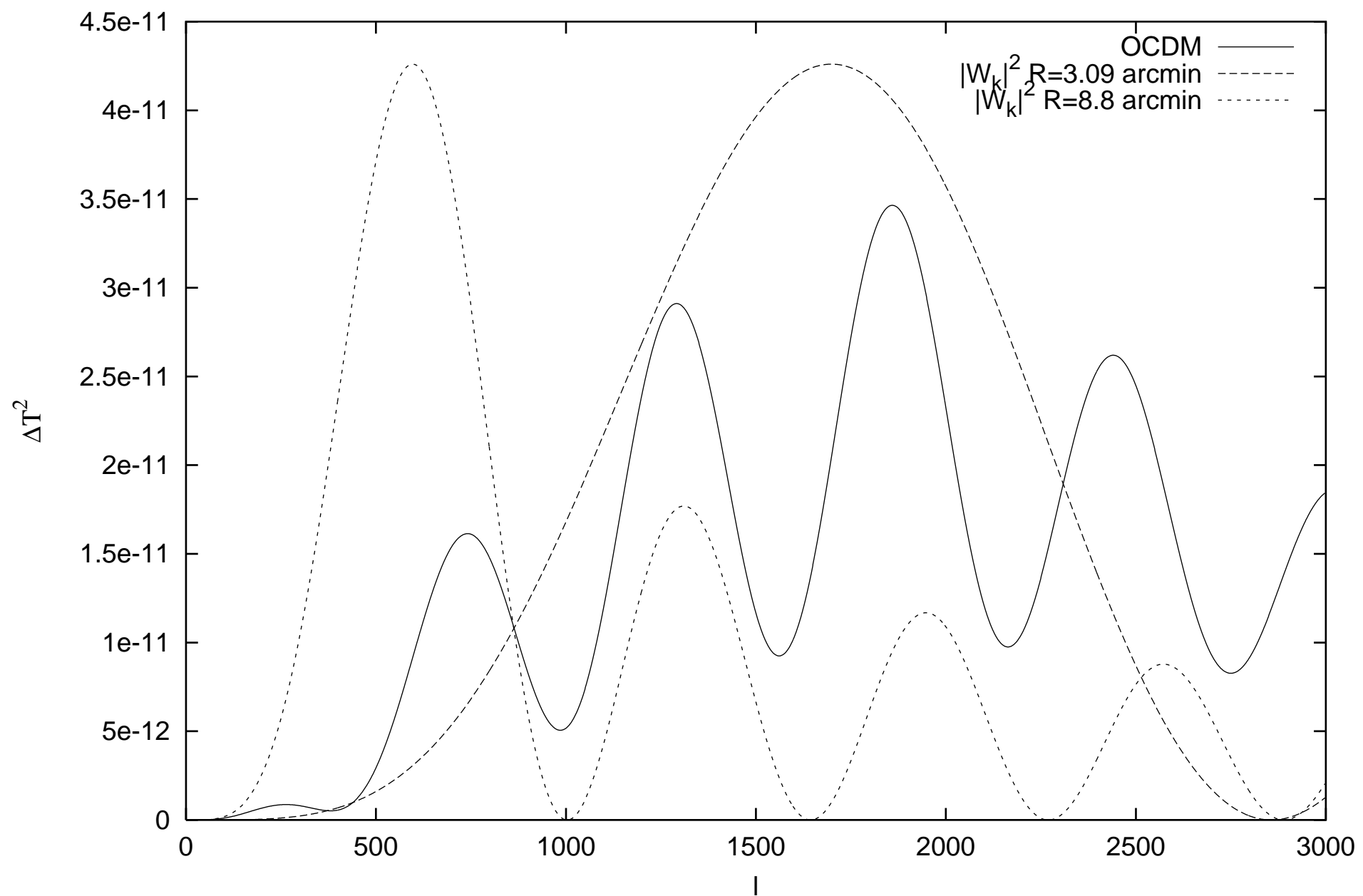


Fig. 2

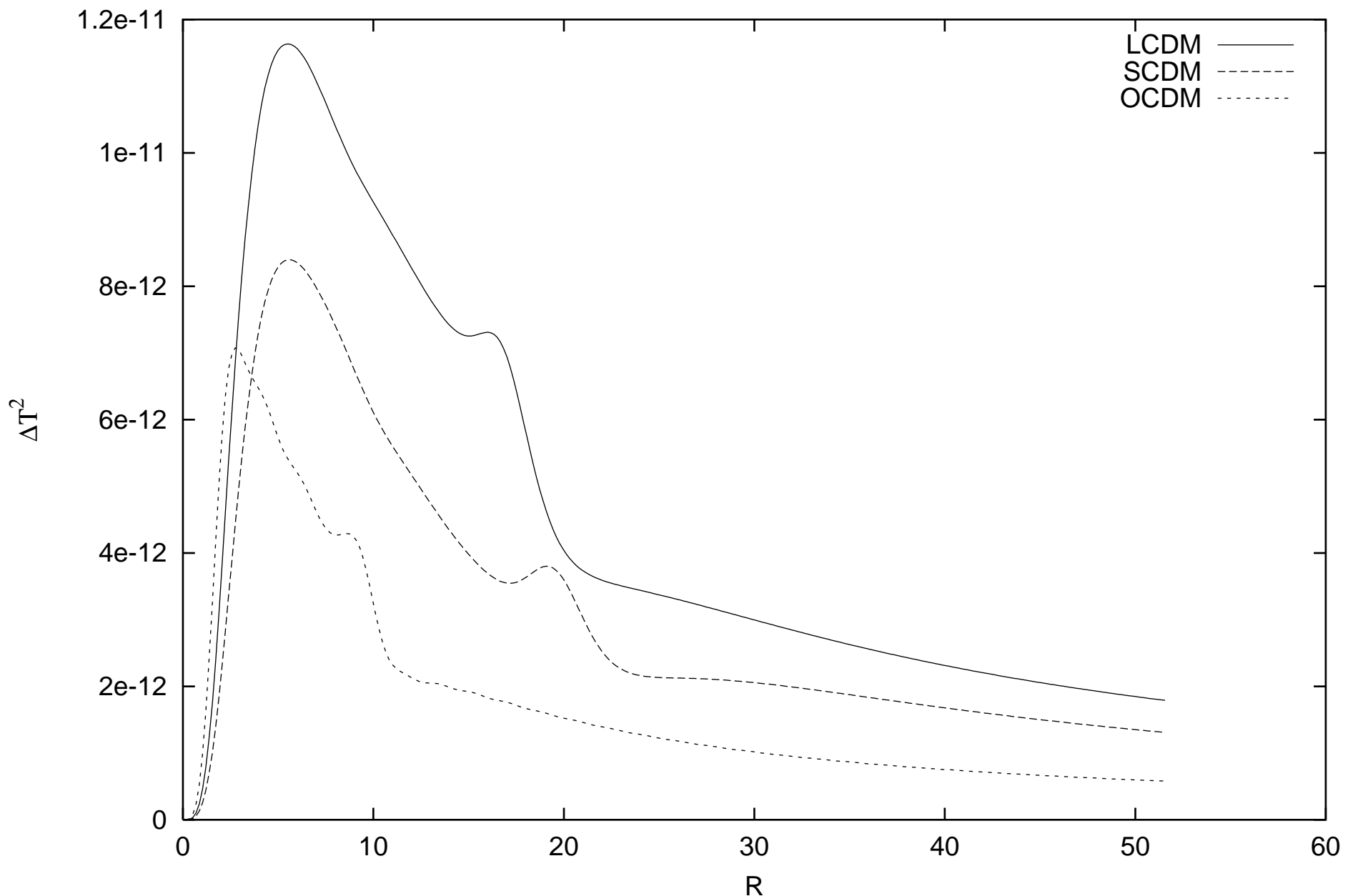


Fig. 3a

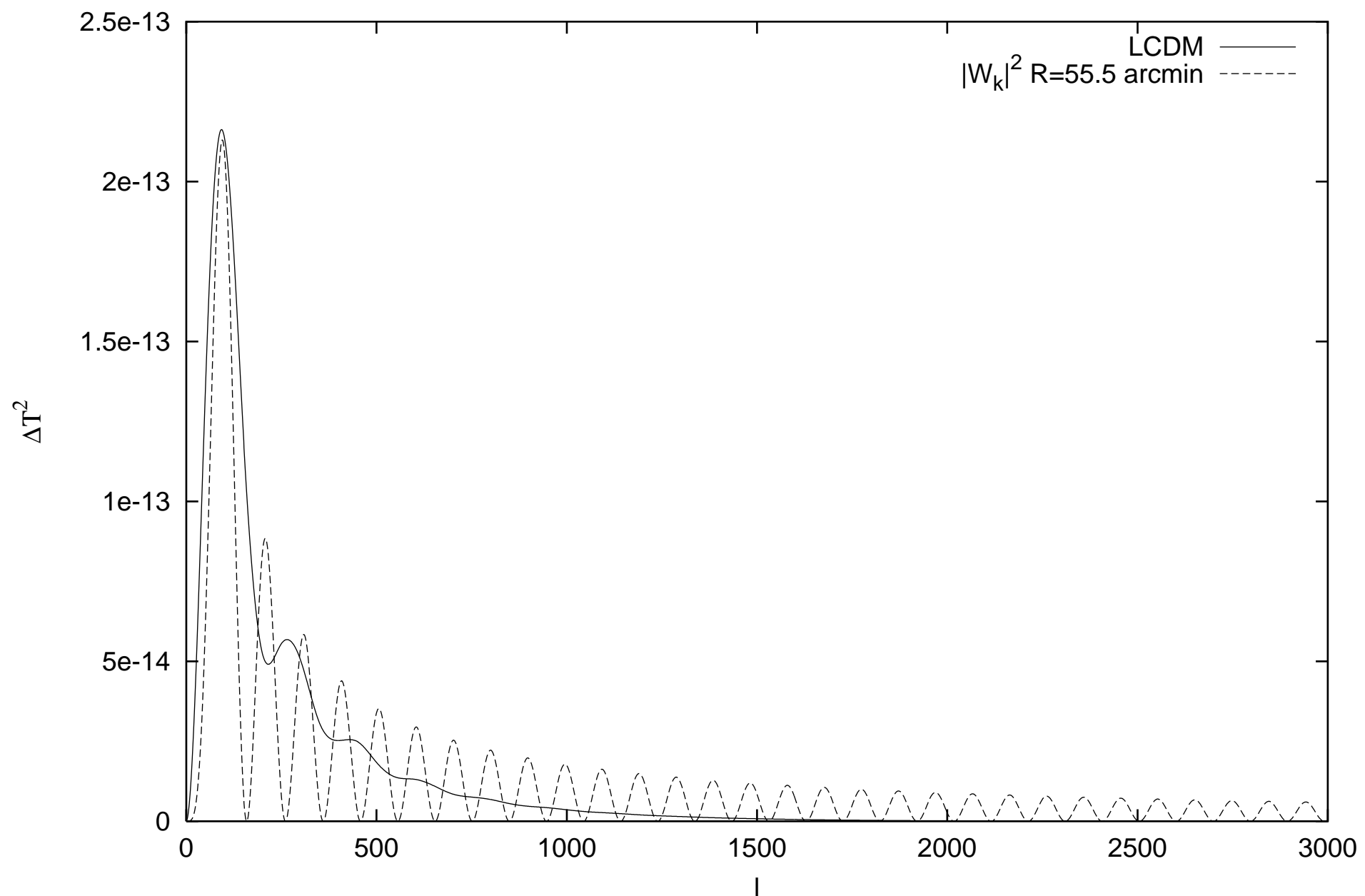


Fig. 3b

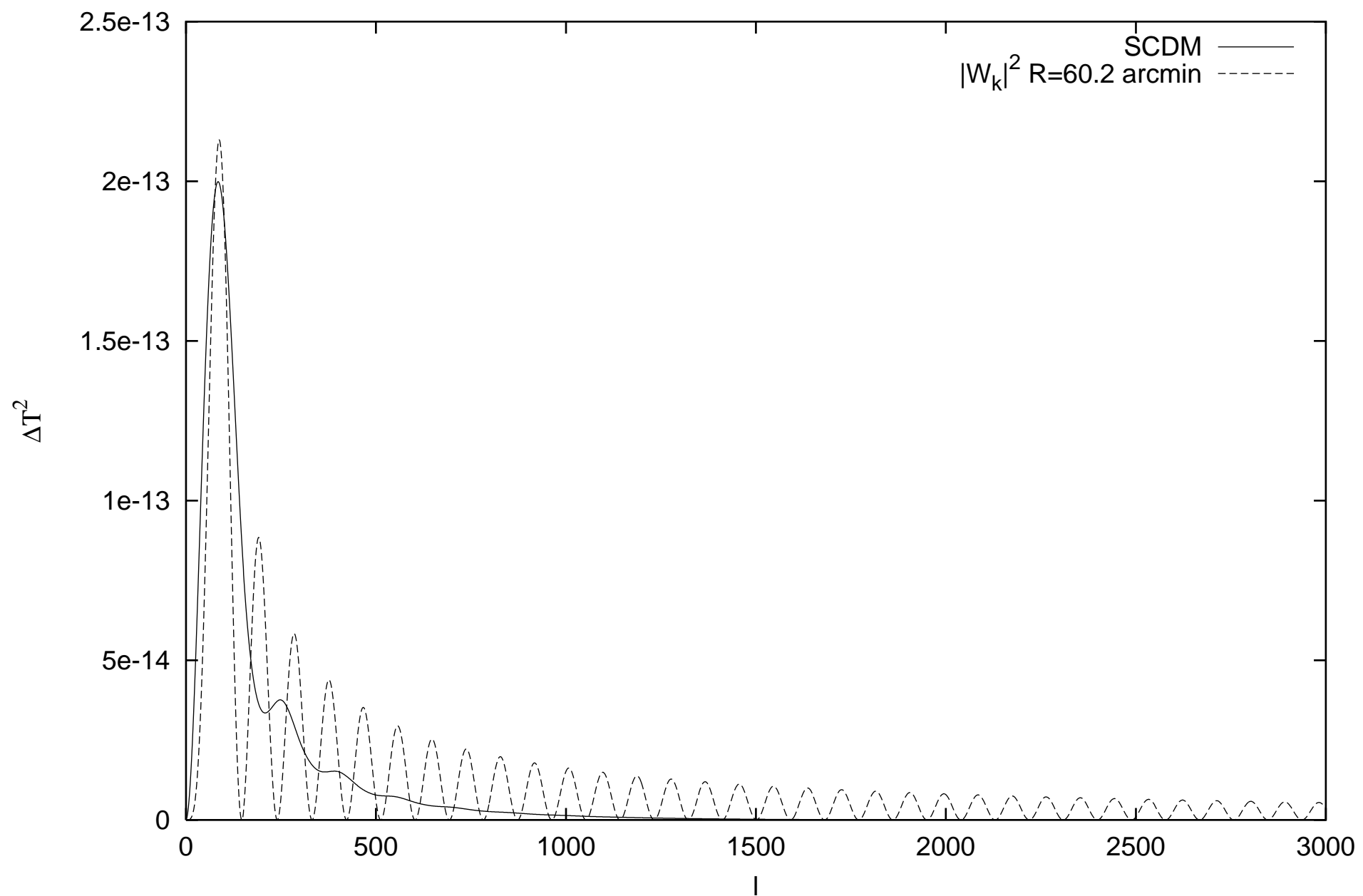


Fig. 3c

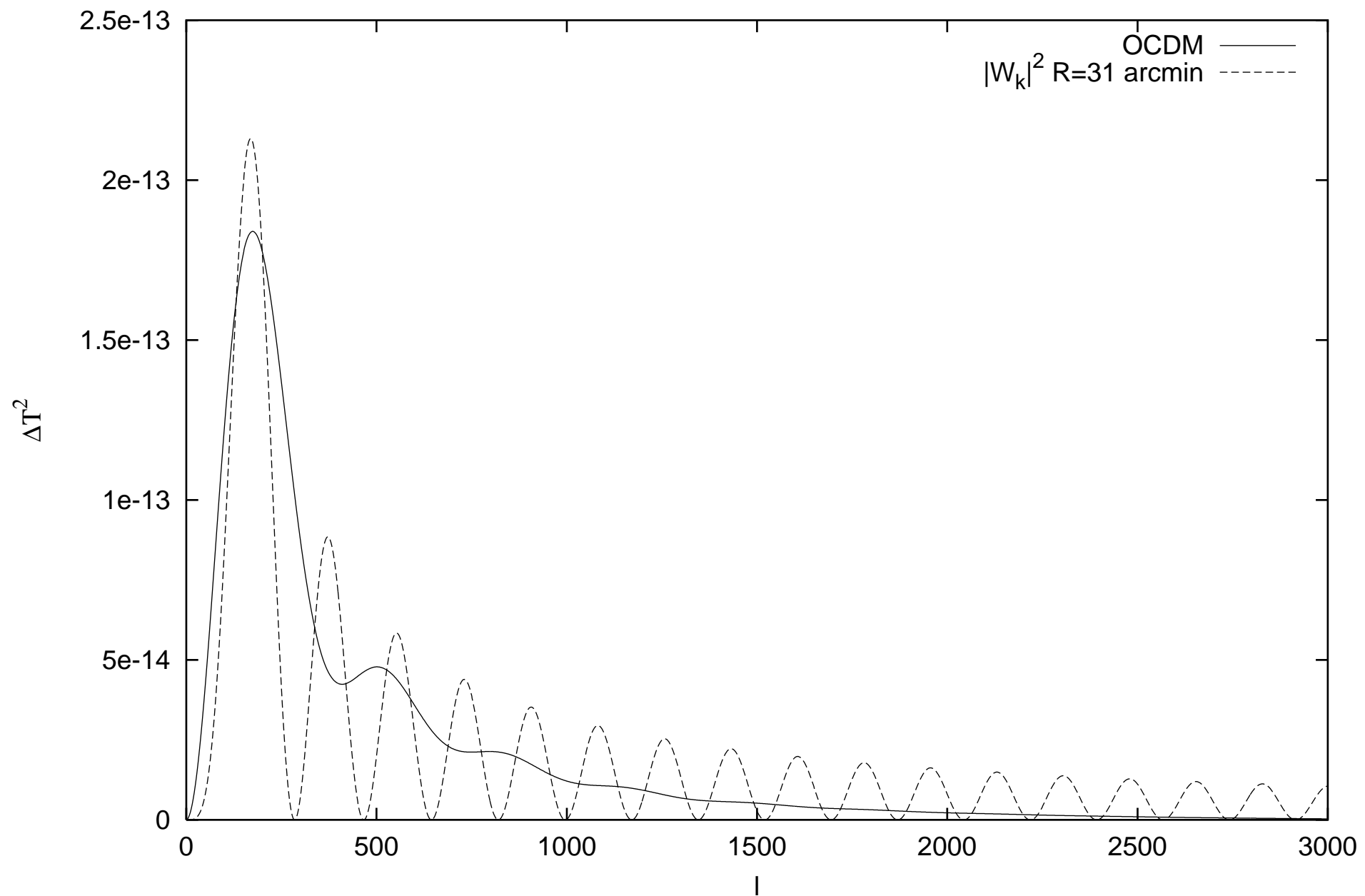


Fig. 4

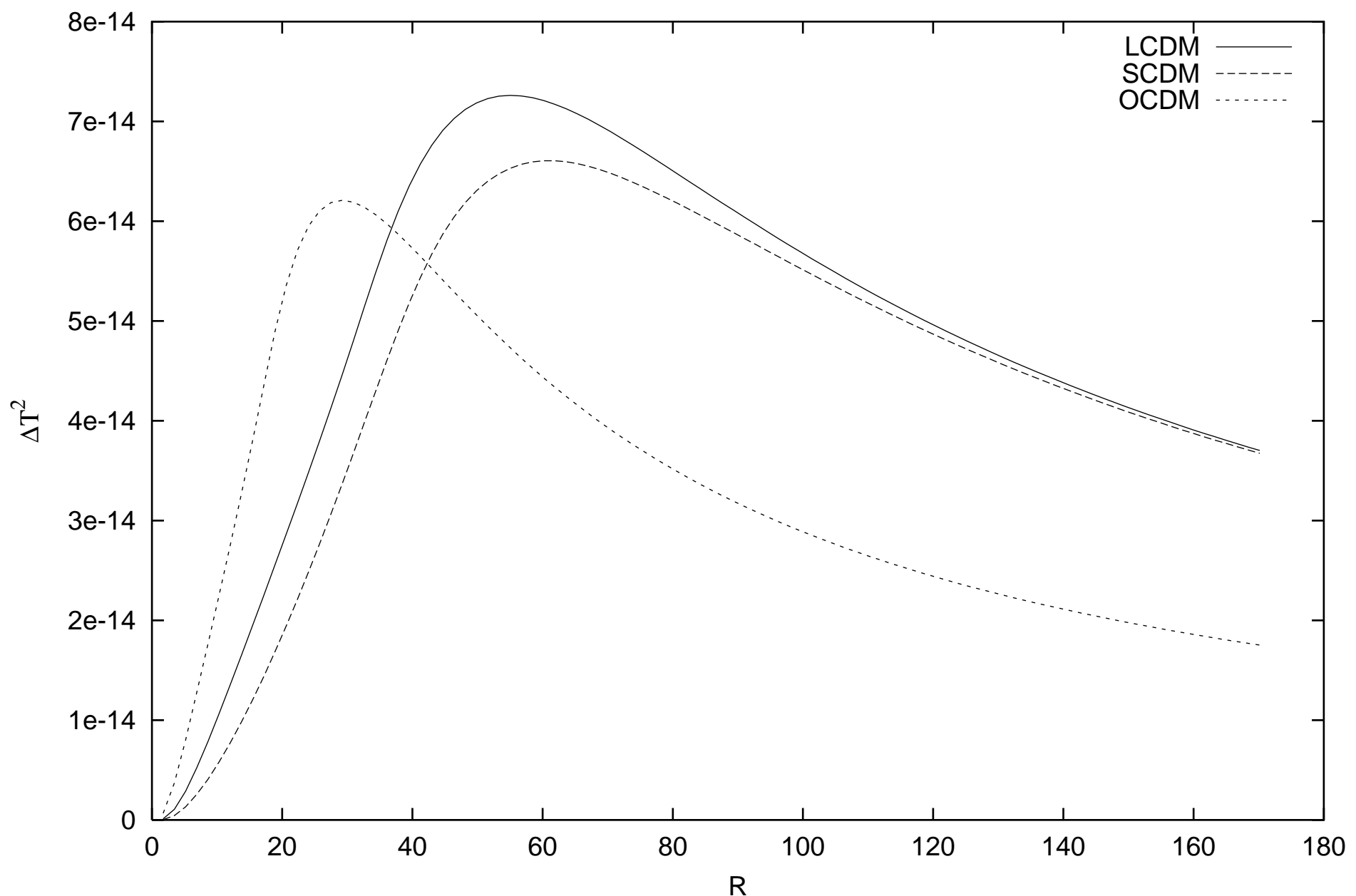


Fig. 5a

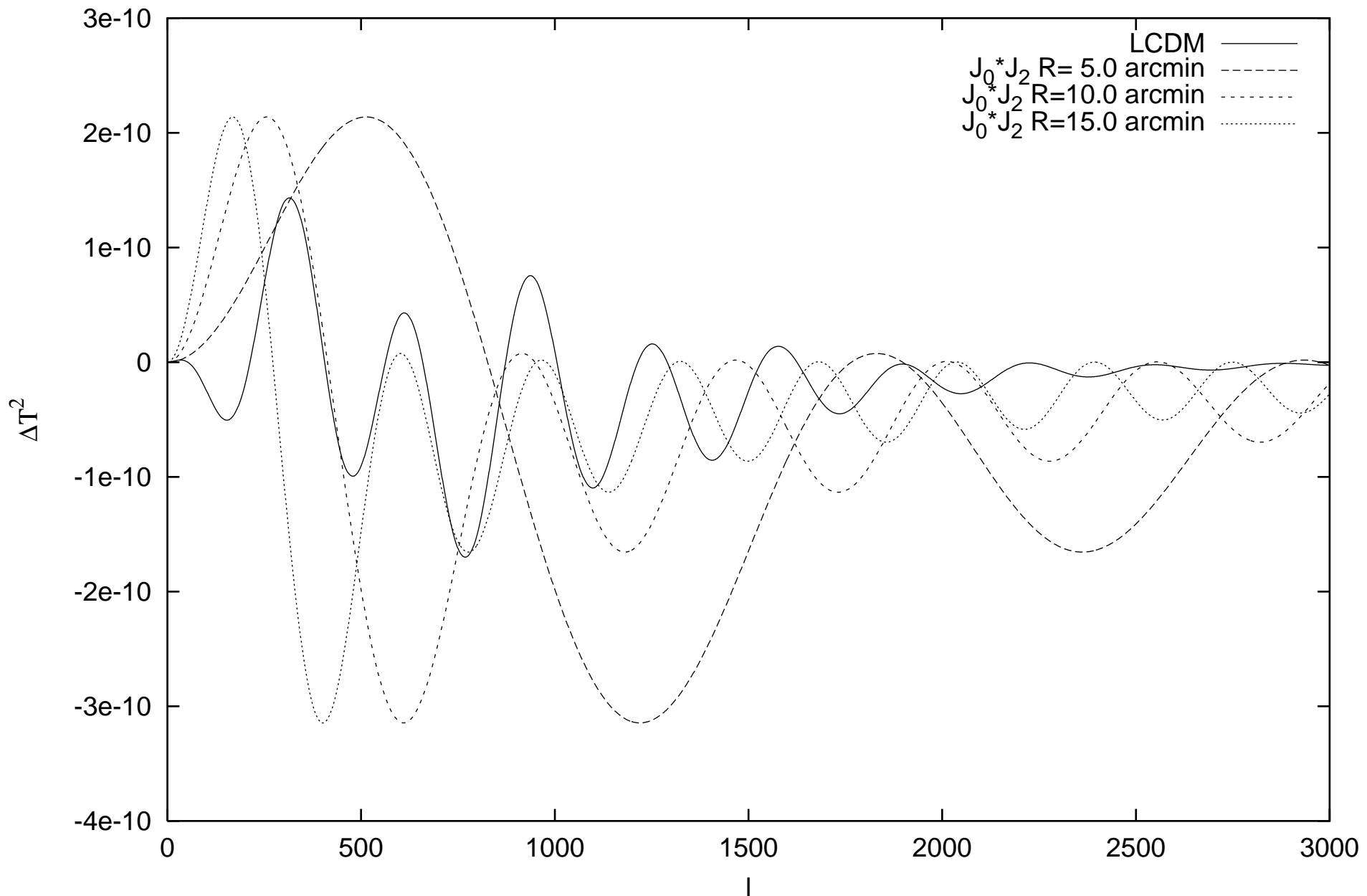


Fig. 5b

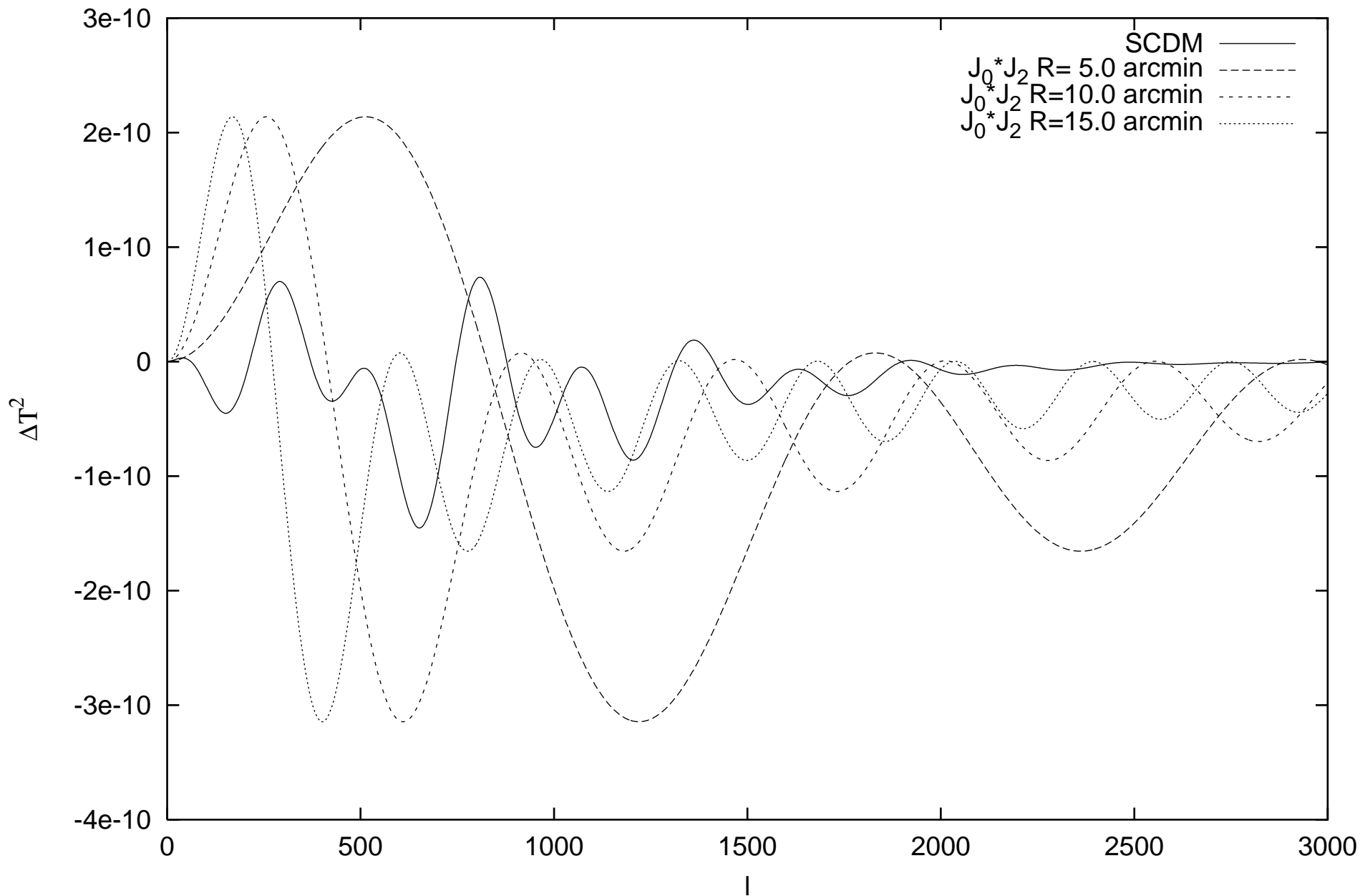


Fig. 5c

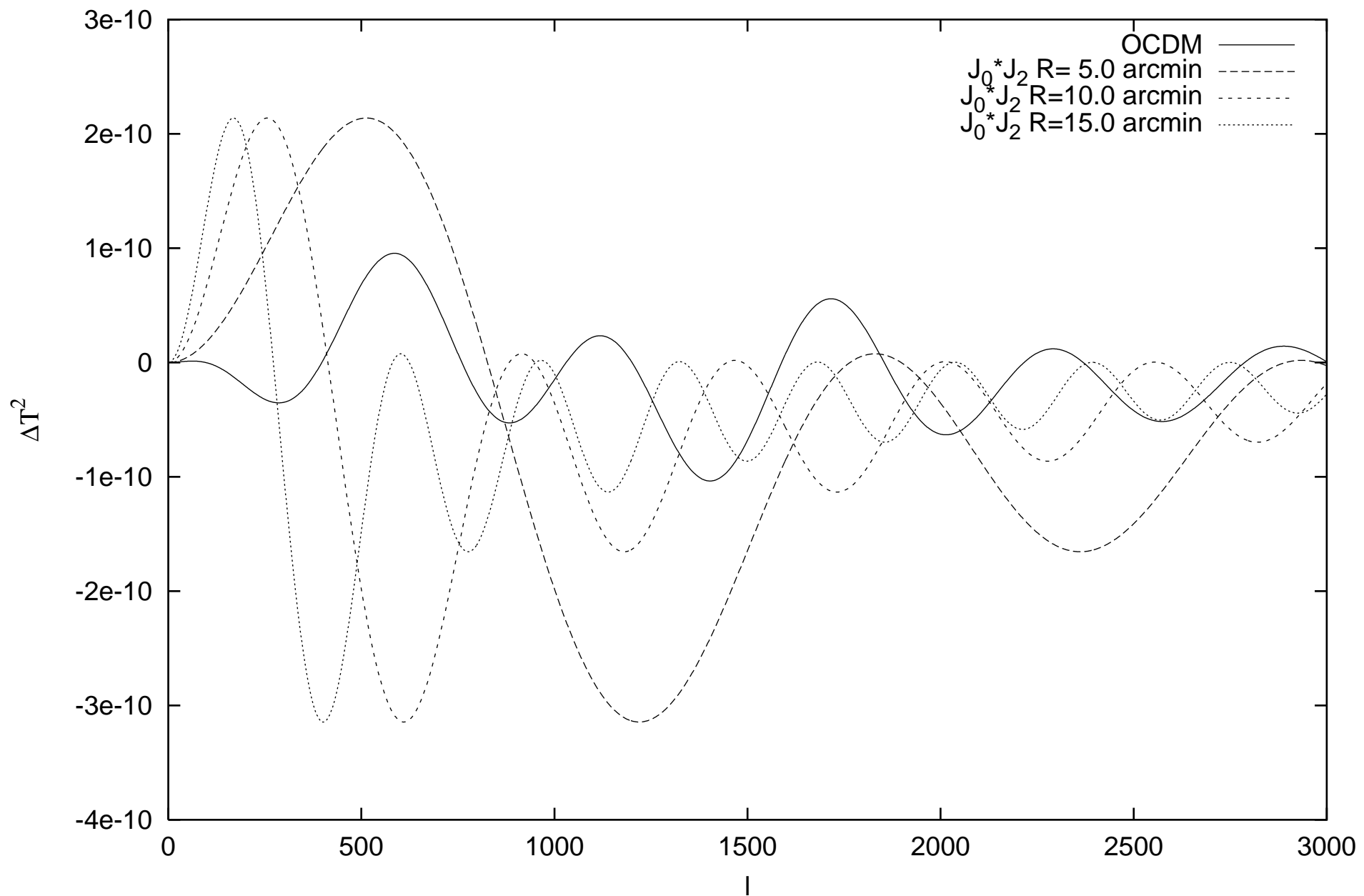


Fig. 6

